



## Chaotic natural convection in a toroidal thermosyphon with heat flux boundaries



W.F. Louisos <sup>a,b,\*</sup>, D.L. Hitt <sup>a,b</sup>, C.L. Danforth <sup>a,c,d</sup>

<sup>a</sup>College of Engineering and Mathematical Sciences, The University of Vermont, United States

<sup>b</sup>Mechanical Engineering Program, School of Engineering, The University of Vermont, Votey Building, 33 Colchester Avenue, Burlington, VT 05405, United States

<sup>c</sup>Department of Mathematics & Statistics, The University of Vermont, 16 Colchester Avenue, Burlington, VT 05401, United States

<sup>d</sup>Vermont Complex Systems Center, Vermont Advanced Computing Core, The University of Vermont, Farrell Hall, 210 Colchester Avenue, Burlington, VT 05405, United States

### ARTICLE INFO

#### Article history:

Received 27 October 2014

Received in revised form 21 April 2015

Accepted 21 April 2015

Available online 15 May 2015

#### Keywords:

Thermosyphon

Toroidal thermosyphon

Natural convection

Unstable convection

Lorenz-like chaos

Rayleigh number ( $Ra$ )

### ABSTRACT

This computational study investigates nonlinear dynamics of unstable convection in a 3D toroidal shaped thermal convection loop (i.e., thermosyphon) with heat flux boundary conditions; results are compared to prior 2D simulations. The lower half of the thermosyphon is subjected to a positive heat flux into the system while the upper half is cooled by an equal-but-opposite heat flux out of the system. Water is employed as the working fluid with fully temperature dependent thermophysical properties and the system of governing equations is solved using a finite volume method. Numerical simulations are performed for varying magnitudes of heat flux ( $1.0 \text{ W/m}^2 \leq q'' \leq 1.0 \times 10^4 \text{ W/m}^2$ ) to yield Rayleigh numbers (i.e., buoyant forcing) ranging from  $2.83 \times 10^4 \leq Ra \leq 2.83 \times 10^8$ . Delineation of multiple convective flow regimes is achieved through evolution of the bulk-mass-flow time-series and the trajectory of the mass flow attractor. Simulation results demonstrate that multiple regimes are possible and include: (1) conduction, (2) damped, stable convection that asymptotes to steady-state, (3) unstable, Lorenz-like chaotic convection with flow reversals, and (4) high Rayleigh, aperiodic stable convection without flow reversals. For the Rayleigh numbers considered, it is observed that certain flow regimes are not accessible in toroidal simulations owing to the constraints of additional surface boundaries in a 3D system. The RMS of mass flow rate, power spectra of oscillatory behavior, dominant oscillatory frequency, and residence time are also described as a function of the buoyant forcing in the system.

© 2015 Elsevier Ltd. All rights reserved.

### 1. Introduction

Natural convection and buoyancy driven dynamic systems exist over a wide range of length scales and are of notable import to the scientific, mathematic, and engineering communities. On a geo-physical scale, counter-rotating convection cells within the asthenospheric layer of the Earth's upper mantle are composed of ductile rock (owing to the extremely high temperatures and pressures) and produce much of the plate tectonic behavior such as the formation of large scale ridges, trenches, and volcanic activity [1]. On a regional scale, Hadley Cells in the planetary atmosphere are intimately related to the behavior of the jet stream via Rossby waves and aid to explain large scale motions of the Earth's atmosphere as well as weather pattern dynamics as quantified by

ensemble averages of teleconnection indices [2]. For example, the North Atlantic Oscillation Index (NAO), which pertains to the North-East US weather, is commonly used by meteorologists to quantify the oscillatory and chaotic fluctuations of the jet stream in an attempt to improve the accuracy of medium range (10–30 days) weather forecasting. On a local scale, convective thunderstorms (derechos, downbursts, and straight-line windstorms), micro-climates, and land/sea breezes are all the result of unstable, differential heating in a thermal-fluid system [3–5]. Examples of natural convection employed in engineered systems include: (1) solar water heaters, (2) nuclear reactors, (3) gas turbine blade cooling, and (4) roads and railways that pass over permafrost, among many others [6–8]. The buoyant forces resulting from thermal gradients within these fluid systems can give rise to complex mass flow circulations and aperiodic behavior.

The nonlinear dynamics of unstable convection have been studied by Lorenz [9] in his 1963 differential equation model for natural convection in Rayleigh–Bénard convection cells. This work has been studied extensively in an attempt to improve mathematical models

\* Corresponding author at: Mechanical Engineering Program, School of Engineering, The University of Vermont, Votey Building, 33 Colchester Avenue, Burlington, VT 05405, United States.

## Nomenclature

$CCW$	counter-clockwise	$Ra$	Rayleigh no.
$CW$	clockwise	$T$	static temperature (K)
$c_p$	specific heat capacity at constant pressure ( $\frac{\text{kJ}}{\text{kg}\cdot\text{K}}$ )	$t$	time (s)
$e$	specific internal energy (kJ)	$\mathbf{v}$	velocity vector (m/s)
$g$	gravitational acceleration ( $\text{m}/\text{s}^2$ )	$\alpha$	thermal diffusivity ( $\text{m}^2/\text{s}$ )
$h$	convection coefficient ( $\frac{\text{W}}{\text{m}\cdot\text{K}}$ )	$\beta$	thermal expansion coefficient (1/K)
$I$	identity matrix	$\theta$	azimuth coordinate (radians)
$k$	thermal conductivity ( $\frac{\text{W}}{\text{m}\cdot\text{K}}$ )	$\tau$	viscous stress tensor (Pa)
$L$	characteristic length scale (m)	$\nu$	kinematic viscosity ( $\text{m}^2/\text{s}$ )
$\dot{m}$	mass flow rate ( $\text{kg}/\text{s}$ )	$\mu$	dynamic viscosity ( $\frac{\text{kg}}{\text{m}^2\cdot\text{s}}$ )
$p$	pressure (Pa)	$\rho$	density ( $\text{kg}/\text{m}^3$ )
$q''$	heat flux ( $\pm\text{W}/\text{m}^2$ )		

of the earth's atmosphere. Physical and/or numerical models such as thermal convection loops, or 'thermosyphons', are a simplified geometry that represents a viable tool for studying the behavior of natural convection cells [10]. Thermosyphons are a useful construct for performing scientific studies as they limit convection to a single, large cell and thus provide the simplest physical model which allows for examination of the various flow regimes that occur in convection cells.

Thermosyphons are fluid systems in which convective flow is induced via buoyant forces that occur when sufficiently large unstable temperature gradients exist (i.e., heating from the bottom and cooling from the top). The fluid circulates within a closed, circular tube (e.g., torus) that is oriented vertically in space with the direction of gravity. The resulting thermal gradient may be accommodated by conduction, or, if the gradient is sufficiently large, buoyancy driven convection. Thermosyphons exhibit many of the typical nonlinear system dynamical effects, particularly, natural convection flow regimes wherein instabilities may grow large and significantly alter the flow behavior within the thermosyphon. The various flow regimes are typically delineated as (1) conduction and/or quasi-conduction, (2) asymptotic, stable convection with unidirectional flow, (3) unstable, Lorenz-like chaotic convection with flow reversals, and (4) high Rayleigh number, aperiodic stable, convection without flow reversals.

Comprehensive review articles written by Yang [11], Raithby and Hollands [12], and Jaluria [13] discuss several important closed-loop thermosyphon problems in various branches of engineering, geophysics, environmental sciences. The review articles [6–13] contain a wealth of literature on theoretical and experimental studies of this simple system, which exhibits typical nonlinear convective effects. Early thermosyphon studies employed 1D models in order to study flow behavior in a thermosyphon with the assumption that all governing parameters are uniform over any given cross section at any moment in time [14,15]. Periodic oscillations were found analytically by Keller [14] in a 1D model consisting of a fluid-filled tube bent into a rectangular shape and standing in a vertical plane. Gorman et al. [16] presented a quantitative comparison of the flow in a thermal convection loop with the nonlinear dynamics of the Lorenz model. Here the system was heated with constant flux over the bottom half and cooled isothermally over the top half. The boundaries of different flow regimes were determined experimentally and the characteristics of chaotic flow regimes were discussed. They also derive a relationship between the parameters of the Lorenz model and the experimental parameters of the fluid and loop. Several flow stability studies have been performed by Vijayan et al. [17] and Jiang et al. [18,19] while Desrayaud et al. [20] completed a numerical investigation of

unsteady, laminar natural convection in a 2D convection loop maintained at a constant heat flux over the bottom half and cooled at a constant temperature over the top half. For a particular range of forcing (i.e., Rayleigh number), it has been observed that the bulk fluid motion in a thermosyphon is chaotic and undergoes flow reversals. Creveling et al. [21] proposed a positive feedback mechanism in order to explain these flow reversals in a thermosyphon.

Within the extensive body of literature pertaining to thermosyphons, only a minimal subset of studies have examined the spatiotemporal behavior of the flow-field dynamics within a thermosyphon. The thermal structure of the flow and velocity-field where characterized in time by Ridouane et al. [22,23] where they examine thermosyphons with isothermal boundary conditions in 2D and 3D geometries. It was found that for 2D thermosyphons, chaotic flow regimes and the associated flow reversals occur for Rayleigh numbers  $9.5 \times 10^4 < Ra < 4.0 \times 10^5$ . However, in the 3D isothermal work [23], flow reversals were not observed for Rayleigh numbers ranging from  $10^3 < Ra < 2.3 \times 10^7$  with isothermal boundaries. Ridouane et al. suggest that 3D flow structures increase flow resistance and thus damp the flow instability mechanism responsible for bulk flow reversals observed in 2D loops.

The basis for exploring the heat flux boundary condition in 3D is driven from multiple fronts. First, the flux boundary provides a better correlation with actual laboratory experiments. And second is the fact that flow reversals were not found in 3D isothermal simulations [23] but are known to occur in experiments with heat flux boundary conditions. In an earlier works by Louisos et al. [24,25] a chaotic flow regime with flow reversals was found in 2D simulations with heat flux boundary conditions. We thus seek to extend this prior work by examining a 3D thermosyphon with toroidal geometry and heat flux boundaries.

The present study considers 3D toroidal thermosyphon simulations with iso-heat flux boundaries: heating on the bottom-half of the loop ( $+q''$ ) and an equal but opposite iso-heat flux cooling on the top half ( $-q''$ ) over the range of Rayleigh numbers from  $2.83 \times 10^4$  to  $2.83 \times 10^8$ . Here we examine both the temporal evolution and the RMS value of the mass flow rate in the thermosyphon. Particular focus is placed on characterizing flow reversals as defined by the transition from clockwise (CW) to counter-clockwise (CCW) flow around the convection loop (or vice versa). The trajectory of the thermosyphon mass flow rate solution is plotted on an attractor diagram and the fixed convective equilibrium solutions are shown as 'orbital centers' for both decaying, periodic, and chaotic flow regimes. A frequency analysis is performed in order to examine the power spectra of the system and

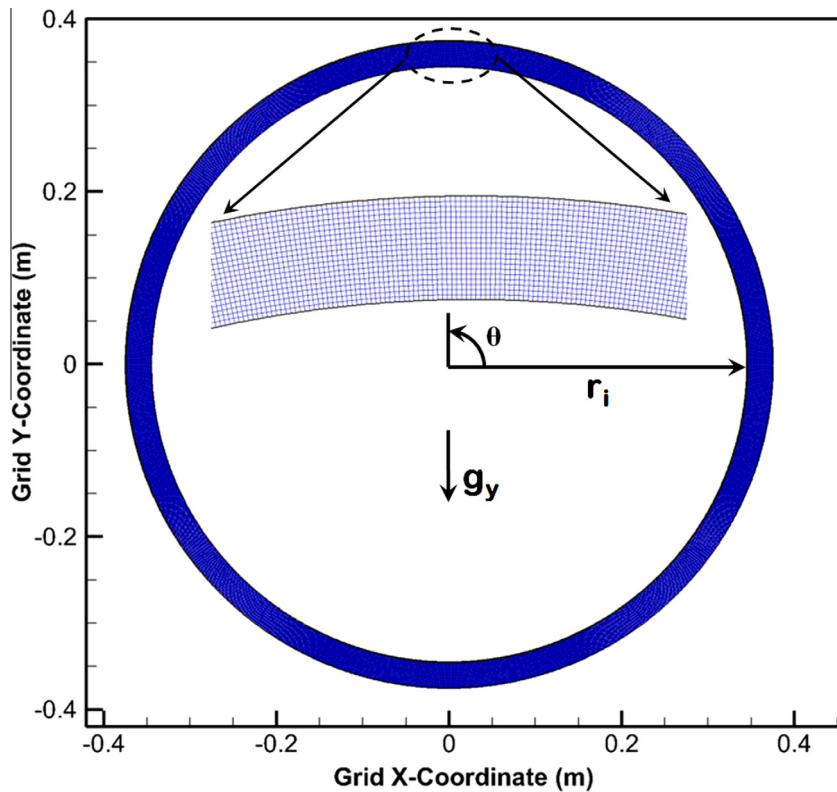


**Fig. 1.** The computational mesh employed in previous 2D thermosyphon studies. The geometry shown provides the starting point for 3D studies.

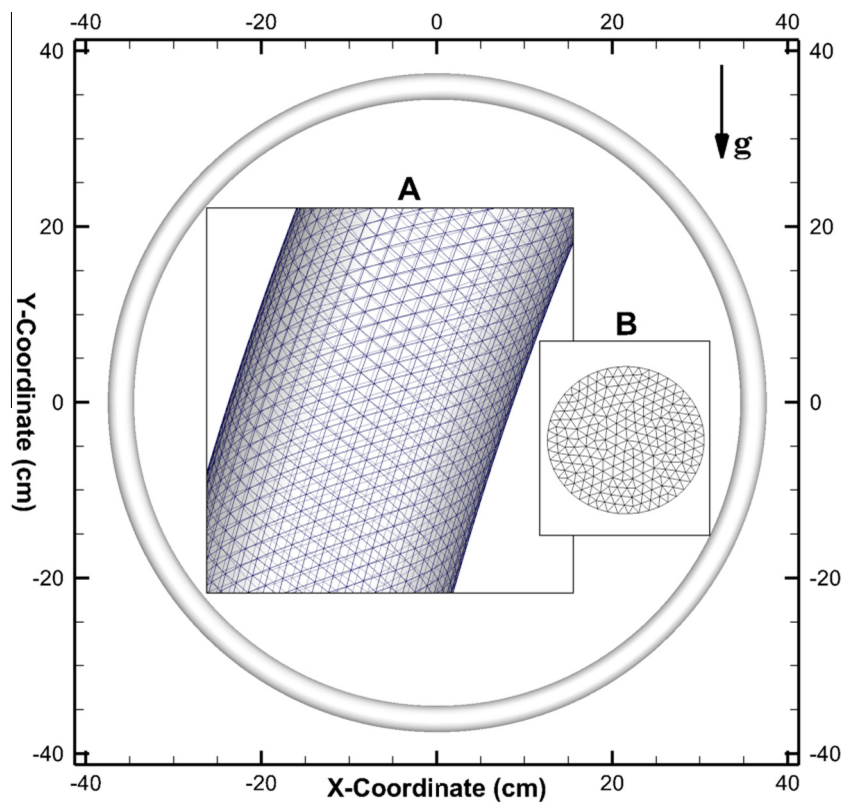


**Fig. 2.** The computational domain employed in 3D thermosyphon simulations. The inset 'A' shows a sample of the numerical mesh around an outer circumferential section of the thermosyphon while the inset 'B' shows the mesh along a typical cross-section.

to determine the dominant frequency and residence time of a particular circulatory direction. Finally, special emphasis is placed on delineating the flow regimes that are encountered as a function of the Rayleigh number.

## 2. Model of physical system

The geometry of the thermosyphon system employed for this study is depicted in Fig. 1 for 2D simulations and in Fig. 2 for 3D simulations. The geometry consists of a closed, circular loop filled with liquid water at atmospheric pressure and oriented in a vertical plane with the force of gravity in the downward direction as shown. The physical dimensions of the loop are 69 cm inner diameter and 75 cm outer diameter; the 3D toroidal thermosyphon has a uniform 3.0 cm cross-sectional diameter.

The initial condition of the thermosyphon system is such that the water is uniformly quiescent throughout the domain and in thermal equilibrium at  $T_0 = 300$  K. In order to create a thermal instability within the closed space, both the inner and outer upper walls ( $0 < \theta < \pi$ ) are imposed with a heat flux ( $-q$ ) out of the system while both the inner and outer lower walls ( $\pi < \theta < 2\pi$ ) are

imposed with an equal in magnitude but opposite direction heat flux ( $+q$ ) into the system. The equal and opposite heat fluxes are held constant along with the acceleration of gravity while the fluid system is monitored as it evolves in time.

In this study, our focus is the delineation of natural convection flow regimes for varying magnitudes of heat flux and gravity as characterized by the Rayleigh number. The Rayleigh number seeks to capture the relative strengths of buoyancy compared to viscous forces multiplied by the ratio of momentum and thermal diffusivity for thermally driven fluid systems. The Rayleigh number is traditionally defined as

$$Ra = \frac{\rho g \beta \Delta T L^3}{\mu \alpha} \quad (1)$$

where  $\rho$  is the fluid density ( $\text{kg}/\text{m}^3$ ),  $g$  is the acceleration of gravity ( $\text{m}/\text{s}^2$ ),  $\beta$  is the thermal expansion coefficient ( $1/\text{K}$ ),  $\Delta T$  is the temperature difference between the hot and cold boundaries ( $\text{K}$ ),  $L$  is the characteristic length scale ( $\text{m}$ ),  $\mu$  is the dynamic viscosity ( $\text{kg}/(\text{m} \cdot \text{s})$ ), and  $\alpha$  is the thermal diffusivity ( $\text{m}^2/\text{s}$ ). In this work with heat flux boundary conditions, as opposed to isothermal boundaries, various combinations of flow parameters (i.e., gravity and heat flux)

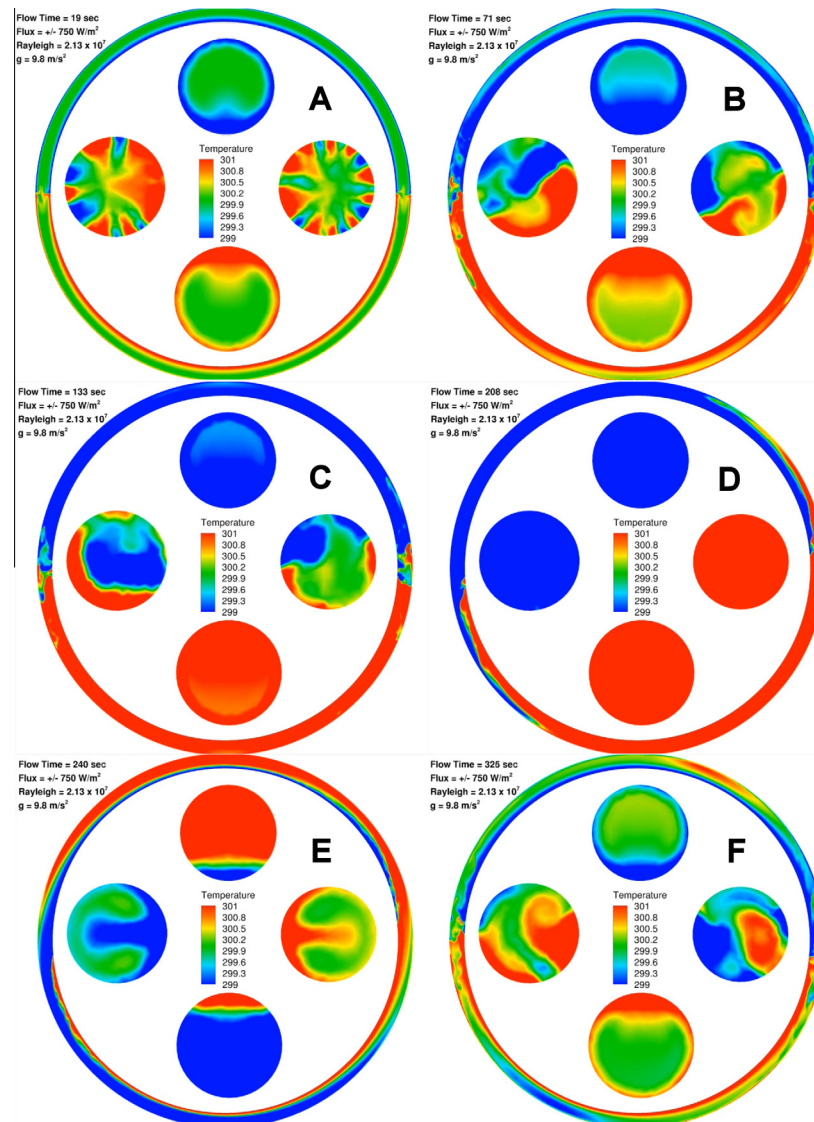


**Fig. 3.** The temperature contours as a function of increasing time from (A) 19 s to (F) 325 s for toroidal thermosyphon flow at  $Ra = 2.13 \times 10^7$ . Note the large magnitude CCW flow shown in (D) at time  $t = 208$  s. As a reference for the reader, a complete animation of this flow-field is provided as a part of the on-line supplemental materials.

may yield the same Rayleigh number. Put another way, a unique set of flow parameters does not exist for a particular Rayleigh number. While the Rayleigh number formulation of Eq. (1) is readily employed for isothermal boundary conditions, it must be modified in order to account for the expected non-isothermal heat flux boundaries in this work. For the case of heat flux boundary conditions, some characteristic temperature differential is required to compute the Rayleigh number. To obtain a representation of the temperature differential, we appeal to Fourier's law of heat conduction

$$q'' = k \frac{\Delta T}{L} \quad (2)$$

in order to estimate temperature difference  $\Delta T$  in terms of the heat flux  $q''(\text{W/m}^2)$  and thermal conductivity  $k(\text{W/(m}\cdot\text{K})$ . This readily provides a redefinition of the Rayleigh number in a form appropriate for the heat flux boundary condition. As such, with  $\Delta T = q''L/k$ , the resulting Rayleigh number formulation used throughout this work is

$$Ra = \frac{\rho g \beta L^4}{\mu \alpha k} q''. \quad (3)$$

This definition of the Rayleigh number in terms of a heat flux boundary has been validated over a large range of forcing conditions (i.e., gravity, heat flux) in prior work [24,25]. Variations of the Rayleigh number are achieved by adjusting the value of the heat flux ( $1.0 \leq q'' \leq 1.0 \times 10^4 \text{ W/m}^2$ ) with the gravitational acceleration ( $0.5 \text{ m/s}^2 < g < 9.8 \text{ m/s}^2$ ) in order to yield Rayleigh numbers ranging from  $1.45 \times 10^3 \leq Ra \leq 2.8 \times 10^8$ .

### 3. Computational methods

The working fluid in this thermosyphon system is liquid water at an operating pressure of one atmosphere (101.325 kPa) and all thermophysical properties, including density ( $\rho$ ), specific heat ( $c_p$ ), thermal conductivity ( $k$ ), and dynamic viscosity ( $\mu$ ), are

modeled as temperature dependent via a piecewise linear function that includes 31 data points.

Computational domains are based the geometry described above and have been generated using Fluent Inc.'s Gambit grid generation software and the numerical grid for 2D simulations is provided in Fig. 1 while the 3D mesh is provided in Fig. 2. A section of the grid on the outer face of the toroidal thermosyphon is provided in Inset (A) of Fig. 2 and the mesh cross-section shown in Inset (B) of Fig. 2 is identically repeated around the entire thermosyphon loop. A formal grid-independence study has been performed for the 3D geometry and follows the procedure as described in Ridouane et al. [22]. The 3D grid sensitivity study yields a final production grid that contains 1.56 million tetrahedral finite volumes with no symmetry assumption. The flow field is governed by the conservation of mass, momentum, and energy according to

$$\frac{\partial}{\partial t} (\rho) + \nabla \cdot (\rho \mathbf{V}) = 0 \quad (4)$$

$$\frac{\partial}{\partial t} (\rho \mathbf{V}) + \nabla \cdot (\rho \mathbf{V} \mathbf{V}) = -\nabla p + \rho(T)g + \nabla \cdot \tau \quad (5)$$

$$\frac{\partial}{\partial t} (\rho e) + \nabla \cdot (\rho \mathbf{V} e) = \nabla \cdot (k \nabla T + (\tau \cdot \mathbf{V})) \quad (6)$$

$$e = c_p T + \frac{1}{2} |\mathbf{V}|^2 \quad (7)$$

$$\tau = \mu \left( (\nabla \mathbf{V} + \nabla \mathbf{V}^T) - \frac{2}{3} \nabla \cdot \mathbf{V} \mathbf{I} \right) \quad (8)$$

where  $e$  is the specific internal energy,  $c_p$  is the specific heat at constant pressure, and  $\tau$  is the Newtonian viscous stress tensor. The no-slip velocity boundary condition is imposed on the inner and outer walls of the computational domain. Owing to the low flow velocities and Reynolds numbers, a laminar viscous model is employed without viscous heating.

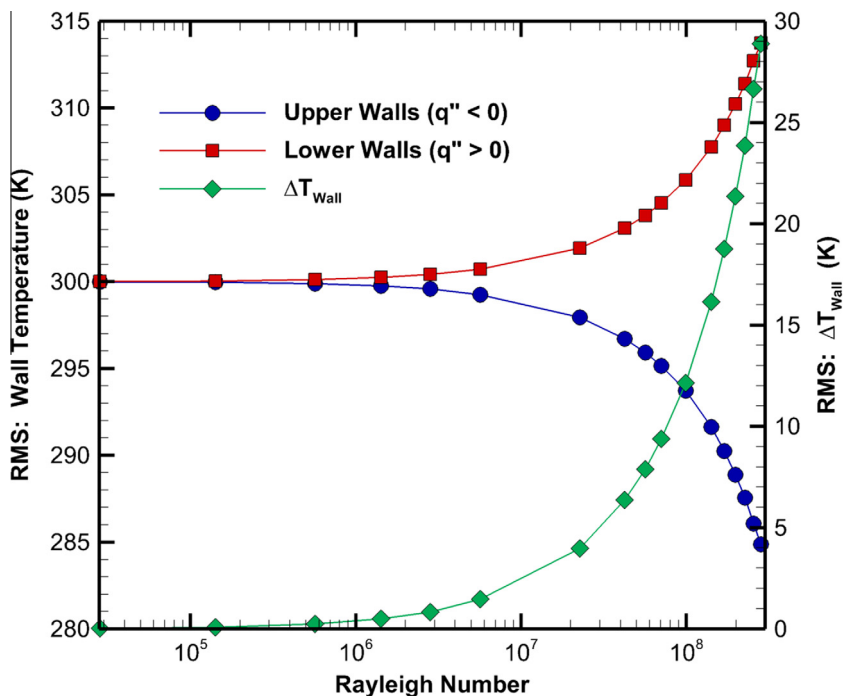
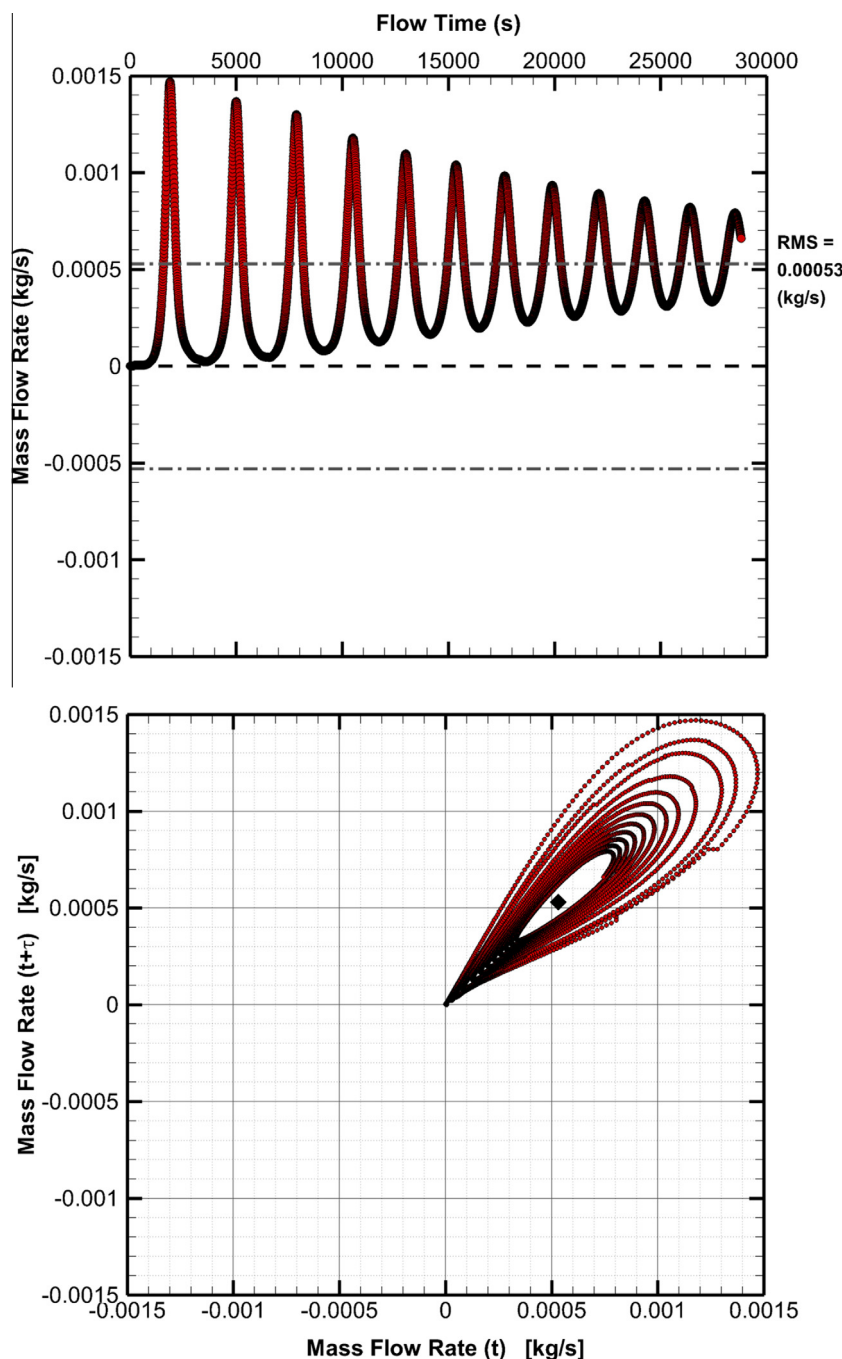


Fig. 4. The RMS value of the measured thermosyphon wall temperature as a function of the Rayleigh number for equal and opposite wall heat flux. Note that  $\Delta T_{wall}$  is also provided as a measure of forcing.

The governing equations are solved numerically using the finite volume method (FLUENT 6.3 [26]). An implicit, pressure-based, segregated solver is employed and all discretization schemes are of second-order accuracy or higher. The QUICK scheme is used for the momentum and energy discretization while the Green–Gauss scheme is used for the spatial discretization. Pressure discretization employs the body-force weighted model and pressure–velocity coupling is handled by the SIMPLE pressure correction algorithm.

In this work, we seek to resolve the temporal evolution of the flow-field from an initial condition of thermal equilibrium at  $T_0 = 300$  K and zero velocity throughout the domain. The unsteady numerical model is second-order implicit in time as utilizes a time-step size of  $\Delta t = 0.25$  s in order to render the solution insensitive to

time-step size. Convergence at each time-step is assessed via computed residuals (mass, momentum, and energy) and flow monitors (e.g.,  $\dot{m}$ ,  $T$ ) at key locations within the domain. The solution at a given time-step is deemed converged when the numerical residuals have fallen below  $10^{-5}$  and flow monitors change by less than 0.01% with further iterations. In this work, we numerically simulate the first 10,000+ s of flow time ( $\geq 40,000$  time-steps) in order to analyze flow-field from start-up at time  $t = 0$  (i.e., thermal equilibrium throughout the domain at a temperature of 300 K and no flow) to the point where the low regime is able to be well characterized. The efficacy of this computational strategy as it pertains to this model of the thermosyphon has been demonstrated in the previous works by Ridouane et al. [22,23] and Louisos et al. [24,25].



**Fig. 5.** The mass flow rate time series (Top) and the associated attractor plot (Bottom) with a time delay  $\tau = 20$  and a heat flux  $q'' = \pm 1.0 \text{ W/m}^2$  ( $Ra = 2.83 \times 10^4$ ). Note that the oscillations decay to the steady, convective RMS value.

#### 4. Results & discussion

In this section, we present and discuss the numerical results from natural convection simulations in a toroidal thermosyphon. First, thermal illustrations and an animation of the flow-field are presented in order to orient the reader. Thermosyphon boundary temperatures along with the  $\Delta T_{\text{wall}}$  are plotted as a function of the Rayleigh number (i.e., iso-heat flux). Next, the mass flow pulsations are provided as a time-series along with the mass flow attractor plot in order to quantify bulk fluid flow as a function of the forcing in the system; the root-mean-square (RMS) of the mass flow rate as a function of the Rayleigh number is also provided. We then discuss the residence time (i.e., CCW vs CW) and perform a frequency analysis of the mass-flow time-series in order to extract dominant oscillatory frequencies and compare the power spectra

of the 3D toroidal thermosyphon to existing 2D data from the literature. Finally, we close this section with a summary of flow regime delineation using a two-parameter bifurcation diagram.

##### 4.1. Overview of flow field characteristics

As a point of illustration and orientation for the reader, typical flow-field characteristics are illustrated in Fig. 3 which portrays the temperature contours in the toroidal thermosyphon for selected time-steps with the forcing corresponding to  $Ra = 2.13 \times 10^7$ . Here we show contours on the vertical  $x$ - $y$  symmetry plane along with cross-sections at the  $\theta = (0, \frac{\pi}{2}, \pi, \frac{3\pi}{2})$  positions. Note that all 6 panels (A–F) in Fig. 3 utilize the same contour color-map scale for comparison purposes.

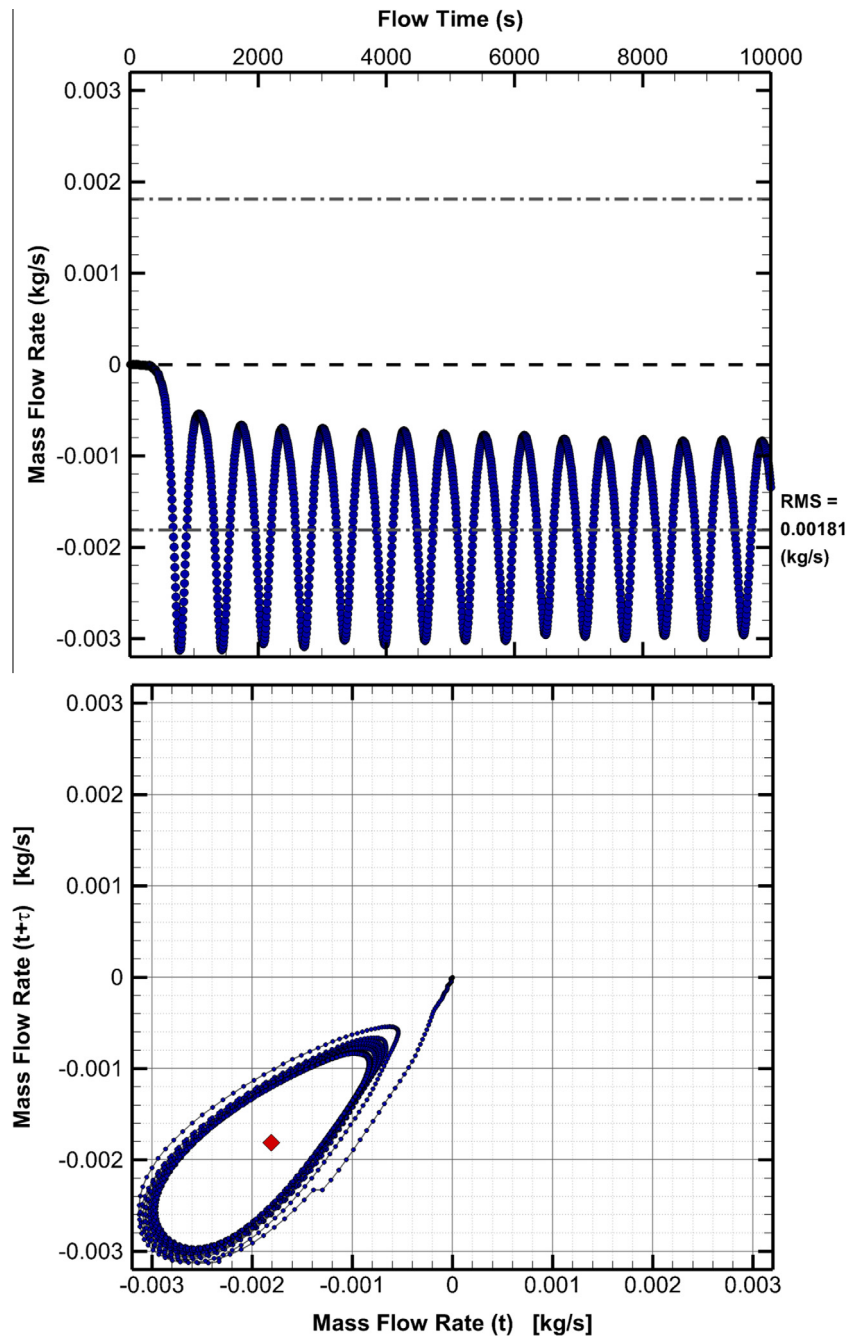


**Fig. 6.** The mass flow rate time series (Top) and the associated attractor plot (Bottom) with a time delay  $\tau = 10$  and a heat flux  $q'' = \pm 20 \text{ W/m}^2$  ( $Ra = 5.67 \times 10^5$ ). Here the oscillations centered on the RMS value approach a stable limit cycle orbiting around the unstable convective equilibrium.

Panel A shows an early time step at time  $t = 19$  s where the flow-field is still nearly isothermal with a small hot layer on the upper-portion of the bottom-half of the thermosyphon and vice versa for the cold layer on the bottom-portion of the upper-half of the loop; this can readily be observed at the  $\theta = \pi$  and  $\theta = \frac{3\pi}{2}$  cross-section insets. Moreover, mixing is observed at the iso-heat flux boundary discontinuity at the  $\theta = 0$  and  $\theta = \pi$  positions where the updraft of warm fluid is mixing with the downdraft of cool fluid. The result is localized, counter-rotating convection cells that distinctly resemble looking ‘downward’ on the well-known Rayleigh–Bénard cellular pattern.

Panels B and C at 71 and 133 s, respectively, illustrate the unstable thermal condition where the buoyant, hot fluid is submerged below the colder, dense fluid on the top; note still the mixing at the  $\theta = 0$  and  $\theta = \pi$  positions. In panel D at 208 s, a large magnitude CCW flow is observed which results in the thermally stable state found in panel E at 240 s with the hot, buoyant fluid above the cold, more dense fluid below.

Finally, in Fig. 3 panel F we see a small, residual oscillation as both the hot and cold fluid ‘pockets’ have surpassed their respective equilibrium positions as the cold fluid is warmed by the incoming heat flux and the hot fluid is cooled by the outgoing heat flux on

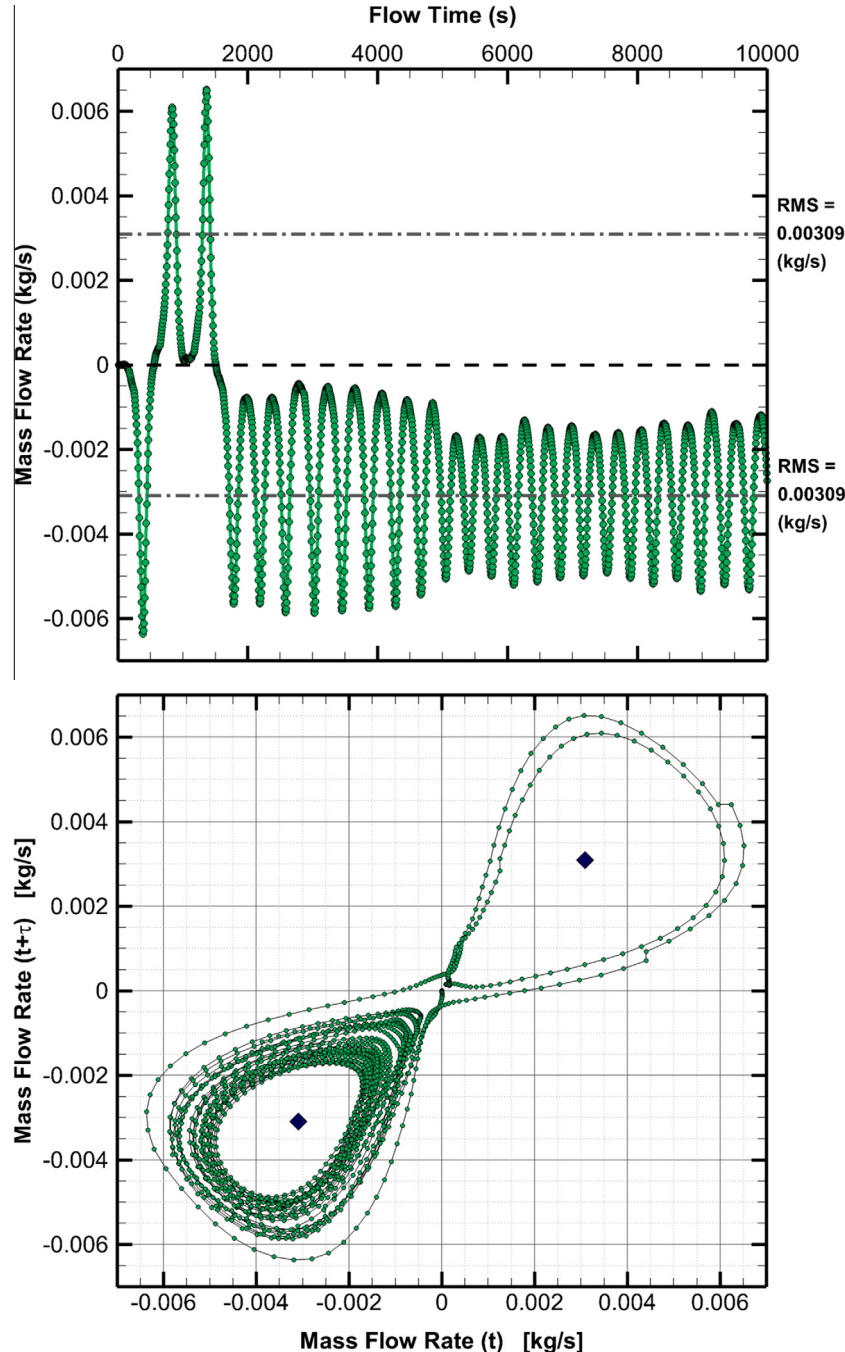


**Fig. 7.** The mass flow rate time series (*Top*) and the associated attractor plot (*Bottom*) with a time delay  $\tau = 10$  and a heat flux  $q'' = \pm 100 \text{ W/m}^2$  ( $Ra = 2.83 \times 10^6$ ). Here, a transient flow reversal is observed and oscillations exhibit a beating pattern.

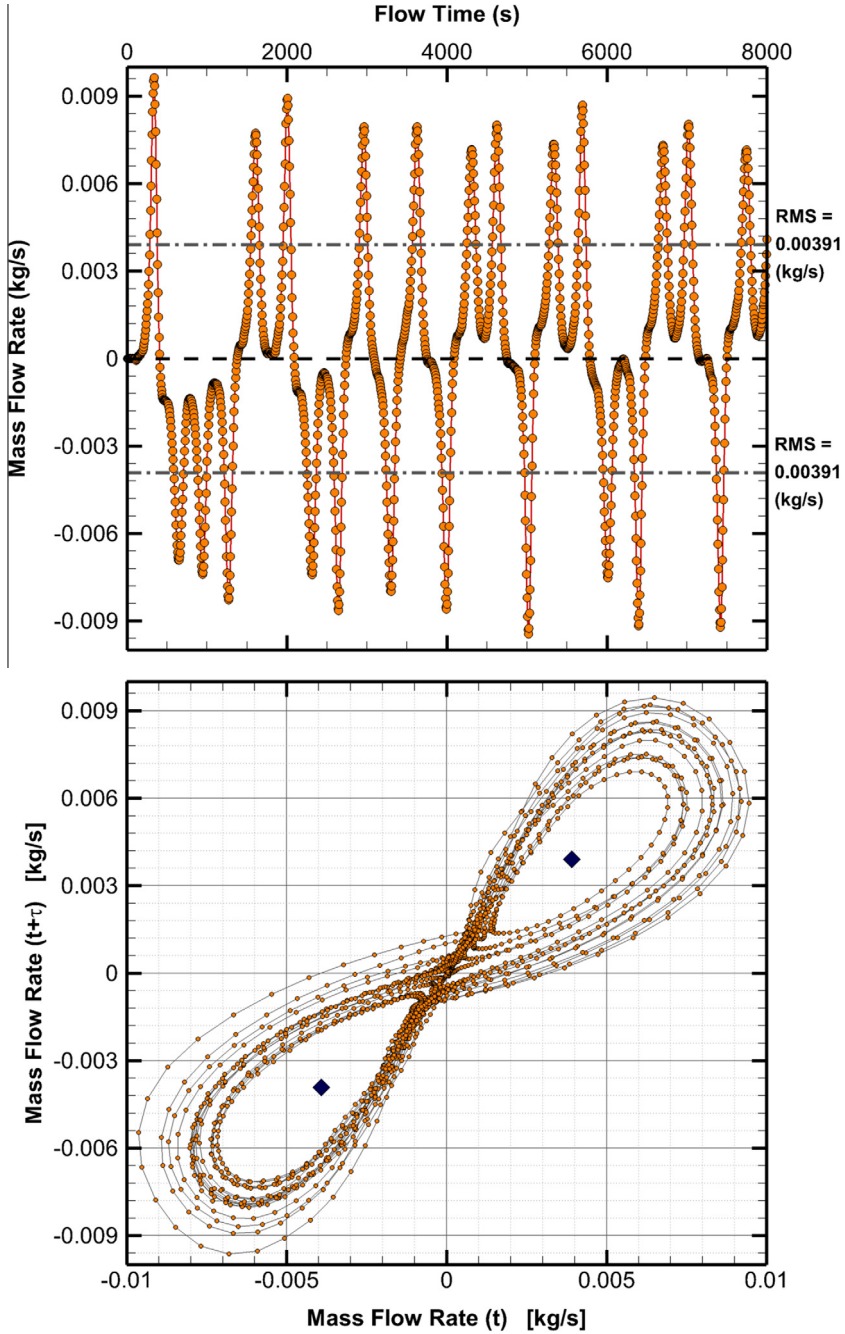


**Fig. 8.** The mass flow rate time series (Top) and the associated attractor plot (Bottom) with a time delay  $\tau = 5$  and a heat flux  $q'' = \pm 200 \text{ W/m}^2$  ( $Ra = 5.67 \times 10^6$ ). This regime demonstrates chaotic flow reversals.

the top-half of the thermosyphon. As a reference for the reader, a complete animation of this flow-field is provided as a part of the on-line supplemental materials.

Forcing within the thermosyphon is numerically controlled via the  $\pm$ iso-heat flux at the thermosyphon wall boundaries, i.e., a larger heat flux generates larger forcing and thus a larger Rayleigh number. As the forcing is increased, it is expected to result in larger mass flow rates which will in turn transport the heat away from the boundaries. In Fig. 4 we characterize the RMS of the thermosyphon wall temperature measured from simulation data as a function of the Rayleigh number; the  $\Delta T_{wall}$  between the heated-lower and cooled-upper wall boundaries is also plotted. This figure provides a reference to the reader and illustrates a “mapping” from the

classically defined Rayleigh number (in terms of  $\Delta T$  (Eq. (1))) to the flux-based form of the Rayleigh number employed in this work (Eq. (3)).

#### 4.2. Temporal dynamics: time series & attractor plots

The typical progression of flow regimes with increased forcing is as follows: (1) pure-conduction and/or quasi-conduction characterized by no bulk circulation and weak, localized mixing at the  $\pm$ heat flux discontinuity; (2) stable convection with continuous, unidirectional bulk mass-flow (i.e., no flow reversals); (3) Lorenz like chaotic flow characterized by oscillations that grow in amplitude with time and result in flow reversals where the bulk mass flow

transitions from CCW to CW and back to CCW many times throughout a given simulation; and (4) high-Rayleigh, stable convection characterized by unidirectional flow with high frequency, low amplitude, aperiodic oscillations centered about a particular mass flow rate [25]. However, for the lowest Rayleigh numbers considered in this study, neither the pure-conduction nor quasi-conduction flow regime was observed. This suggests that a conduction dominated regime in 3D thermosyphons exists at a forcing with  $Ra < 2.83 \times 10^4$ .

Moreover, a significant disparity between the 2D and 3D simulations is that a high-Rayleigh, stable convective regime is not observed in 3D toroidal thermosyphon simulations up to a Rayleigh number of  $Ra = 2.83 \times 10^8$ . In 2D simulations, the

high-Rayleigh, stable flow regime was found at Rayleigh numbers as low as  $10^7$ . We mention here that thermosyphons with  $Ra > 10^8$  were not considered in this work owing to the fact that localized regions in the flow were shown to reach their saturation temperature and thus result in a phase change (freezing/boiling) that is not compatible with the current model.

The temporal evolution of the mass-flow-rate time-series and the associated attractor plots are presented in Figs. 5–10 for the toroidal thermosyphon as the Rayleigh number is increased from  $2.83 \times 10^4$  to  $5.67 \times 10^7$ . It is important to note that in Figs. 5–10 the ordinate axis in the time-series plots (mass flow rate) and both axes in the attractor plot are scaled so as to provide detailed resolution of the oscillatory flow evolution.

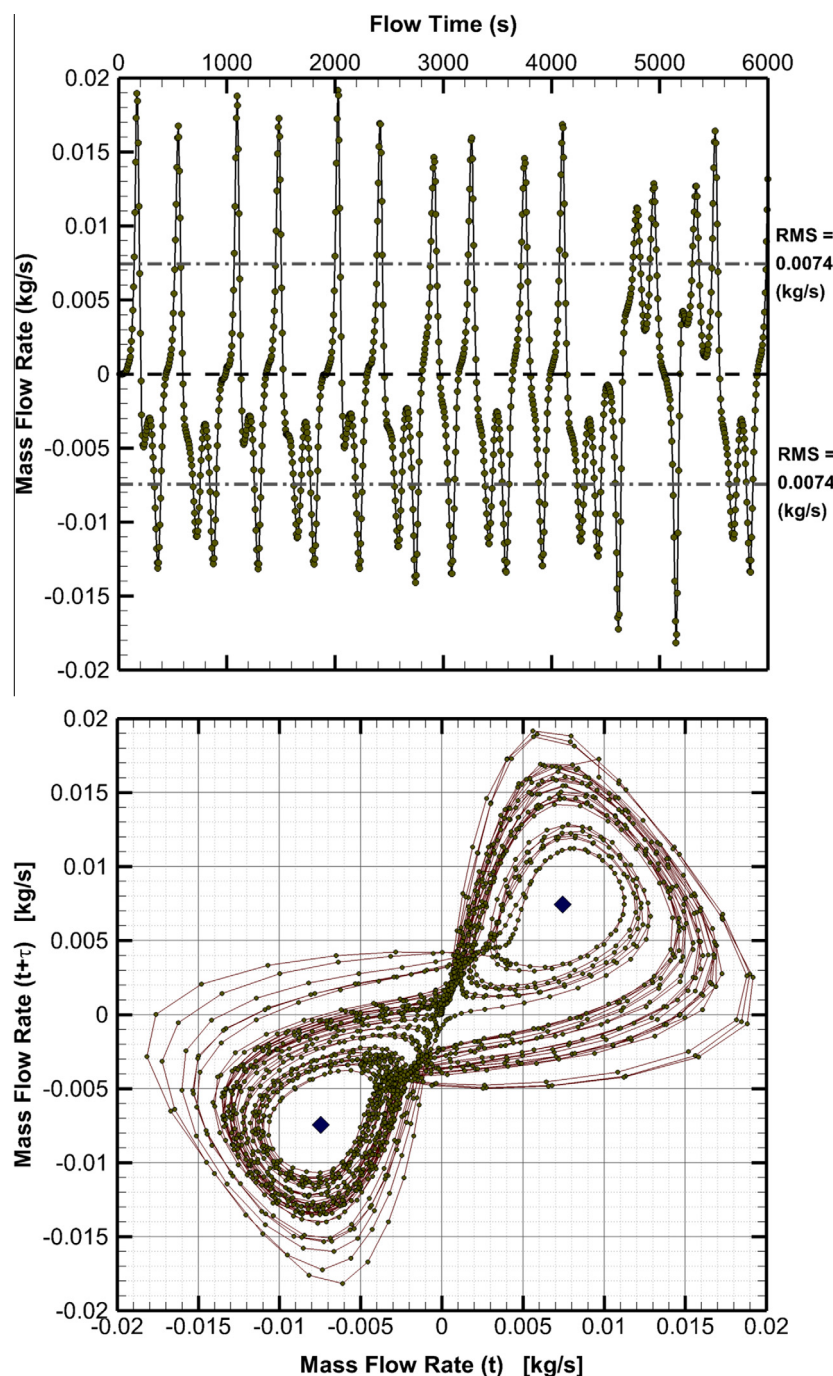


**Fig. 9.** The mass flow rate time series (Top) and the associated attractor plot (Bottom) with a time delay  $\tau = 5$  and a heat flux  $q'' = \pm 800 \text{ W/m}^2$  ( $Ra = 2.27 \times 10^7$ ).

**Fig. 5** shows a typical stable convective flow regime with damped oscillations that asymptote to a steady-state RMS value. The attractor plot (Fig. 5, bottom) shows the measured state variable (mass flow rate) experiencing an inward-spiraling, degrading orbit with sequentially smaller radii upon each orbit; the state variable will eventually land on the RMS value and experience steady, stable convection in perpetuity.

**Fig. 6** illustrates the behavior of a system with oscillations that are centered on the RMS value and approach a stable limit cycle that orbits around the unstable convective equilibrium. The behavior shown in **Fig. 7** is very similar to that of **Fig. 6** save for the fact that a flow reversal is observed along with a subsequent

“beating” pattern. As such, **Fig. 7** represents a flow regime that is transitional between steady convection and chaotic behavior.

**Figs. 8–10** illustrate the classic Lorenz chaotic behavior. As the forcing is increased within this regime, flow reversals become more frequent and the orbital patterns of the attractor plot become more dispersed. However, immediately following a flow reversal, the orbiting state variable tends to approach the RMS value much more closely – and with small amplitude oscillations – before the orbiting radii increases and the system is yet again thrown into a reversed flow direction. This is in direct contrast to the low forcing cases where the orbit decays to the steady RMS value and the stable, oscillatory cases where the orbiting radii remains nearly constant.

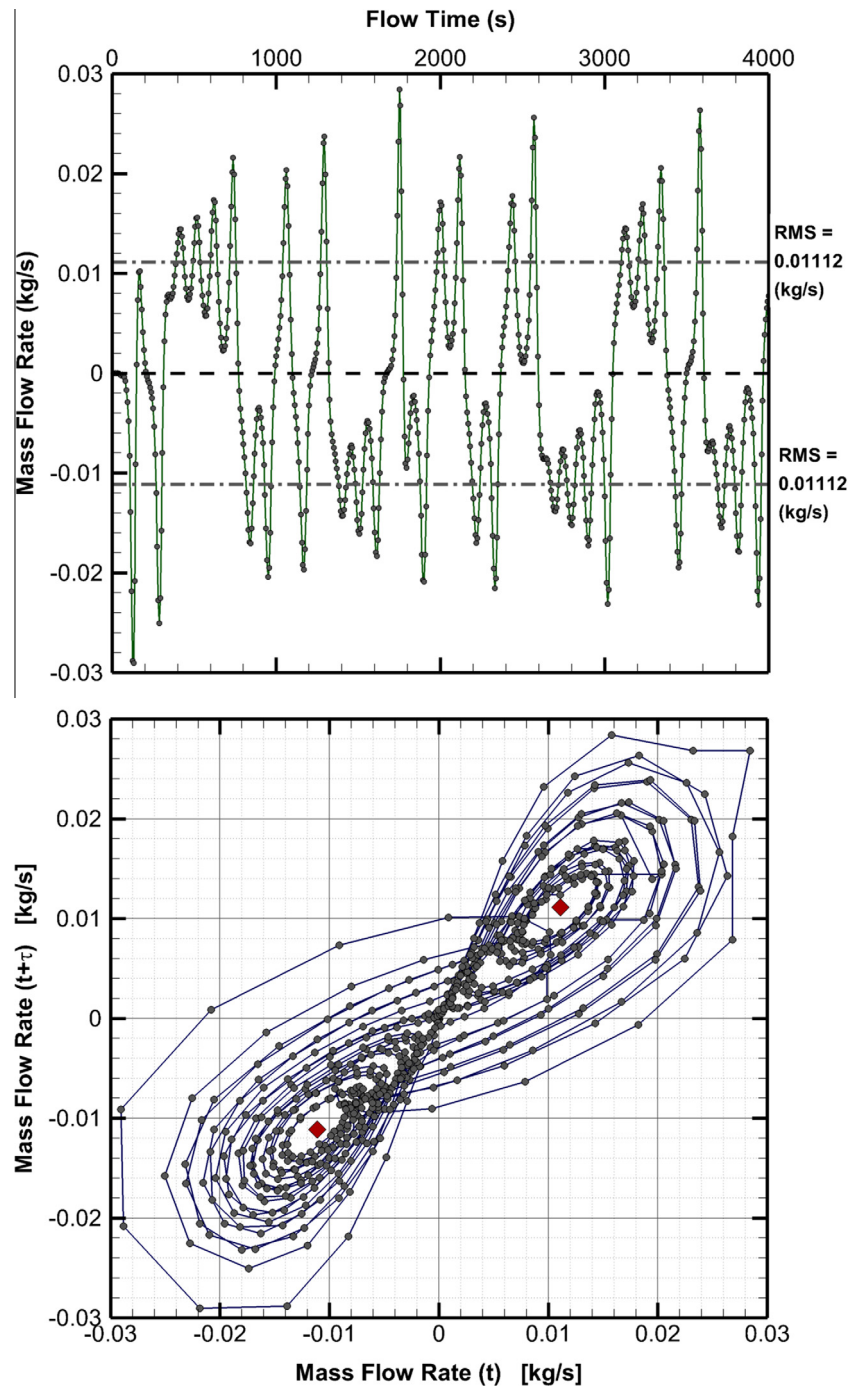


**Fig. 10.** The mass flow rate time series (Top) and the associated attractor plot (Bottom) with a time delay  $\tau = 2$  and a heat flux  $q'' = \pm 2000 \text{ W/m}^2$  ( $Ra = 5.67 \times 10^7$ ). This regime demonstrates chaotic flow reversals.

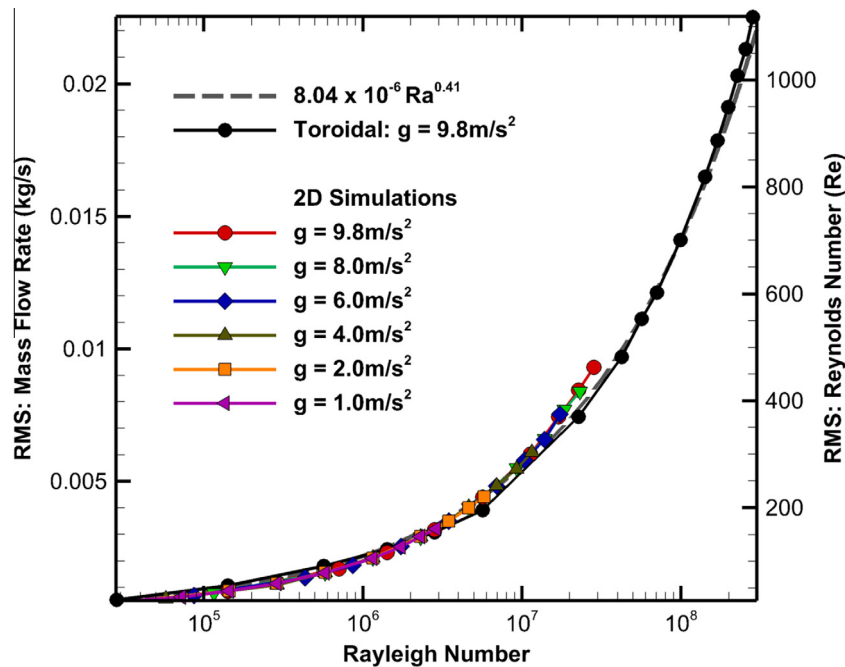


**Fig. 11.** A semi-log plot of the RMS of the mass flow rate signal for both 2D and 3D simulations as a function of the Rayleigh. Note that the RMS of the mass flow rate scales as  $\dot{m} \sim Ra^{0.41}$ .

For the Lorenz-like chaotic flow regimes, the attractor plot shows an initially small radius orbital that grows larger with time until a flow reversal is achieved; it is this growing orbital radii that generates the appearance of a dispersed attractor plot.

We now demonstrate the sole dependency of the flow behavior on the dimensionless Rayleigh number for both 2D and 3D toroidal thermosyphons. To do so, the results of all parametric cases (i.e., all values of  $g$ ,  $q''$ ) have been used to calculate the RMS value of the mass flow rate from the time-series of Figs. 5–10 as a function of the Rayleigh number. The RMS values of mass flow rate, along with the RMS of the Reynolds number, is plotted in Fig. 11. Here we see the collapse of the RMS time-series mass-flow signal onto a single curve which captures both 2D and 3D behavior up to  $Ra = 10^8$ . Also shown is an exponential curve-fit as  $Ra^{0.41}$  on a semi-log plot (regression coefficient of 0.98) which is consistent with power law scalings found in typical natural convection systems with internal flow [27].

#### 4.3. Frequency analysis & residence time

In this section, we turn our attention to the frequency characteristics of the flow pulsations and flow reversals observed in the time-series data of Figs. 5–10. The mass flow rate is used as the input signal to a Fourier transform and power spectra have been computed for each of the cases. Fig. 12 shows representative power spectra for selected thermosyphon flow regimes. The computational parameters implemented in this study (time-step size, data reporting interval) allow the power spectra to capture frequencies up to  $8.0 \times 10^{-2}$  Hz. This is approximately 1/10–1/40 of the average time required for a fluid particle to circulate once around the entire thermosyphon circumference depending on the particular strength of the forcing and the convective flow rate.

Fig. 12(A) corresponds to the mass flow signal shown in Fig. 5 ( $Ra = 2.83 \times 10^4$ ) and is representative of convective flow with damped, asymptotic oscillations that decay to steady-state convection equal to the RMS value of the mass flow rate. The dominant oscillatory frequency is well defined at  $4 \times 10^{-4}$  Hz and the power

spectrum rapidly weakens at frequencies greater than  $10^{-3}$  Hz. Fig. 12(B) corresponds to the mass flow signal of Fig. 7 ( $Ra = 2.83 \times 10^6$ ) and is representative of a flow regime that is transitional between stable and unstable convection. Here the peak in the power spectrum is less pronounced and shifted to a higher frequency ( $2.5 \times 10^{-3}$  Hz) while the amplitude of the spectrum has increased in the higher frequency range.

The power spectra of chaotic natural convection is shown in Fig. 12(C) and (D) for Rayleigh numbers corresponding to  $2.27 \times 10^7$  and  $2.27 \times 10^8$ , respectively. In this flow regime, the power spectra do not exhibit a dominant frequency but rather a broad-bandwidth from the lowest frequencies and up to greater than  $10^{-2}$  Hz. This is a notable characteristic of 3D thermosyphons that is not observed in the 2D counterparts.

When considering Fig. 12 we note two observations: First, at low forcing, the dominant frequency is low and rather pronounced while the power spectrum exhibits a rapid drop in amplitude at higher frequencies. And second, as the forcing in the system increases, there is not a well defined, dominant oscillatory frequency but rather a broad-band power spectra is observed which weakens only at very high frequencies. This is a notable disparity from prior 2D simulations detailed in Louisos et al. [25] where the dominant oscillatory frequency is more pronounced at higher forcing. We now turn our attention to a comparison of 2D and 3D thermosyphon results wherein both the similarities and disparities are explored in further detail.

The dominant oscillatory frequency has been extracted from the power spectra and is plotted as a function of the Rayleigh number in Fig. 13. Here is observed that the 2D and 3D cases share a nearly identical behavior for  $Ra \leq 2.83 \times 10^6$  at which point the trends noticeably diverge. The dominant frequency is coincident and increasing with Rayleigh number for both cases until the toroidal geometry begins to reveal chaotic behavior. At this point, the 3D toroidal thermosyphon no longer exhibits a well-defined dominant frequency but instead enters a region of broad power spectra. The 2D thermosyphon on the other hand maintains the trend while the dominant frequency actually becomes more pronounced.

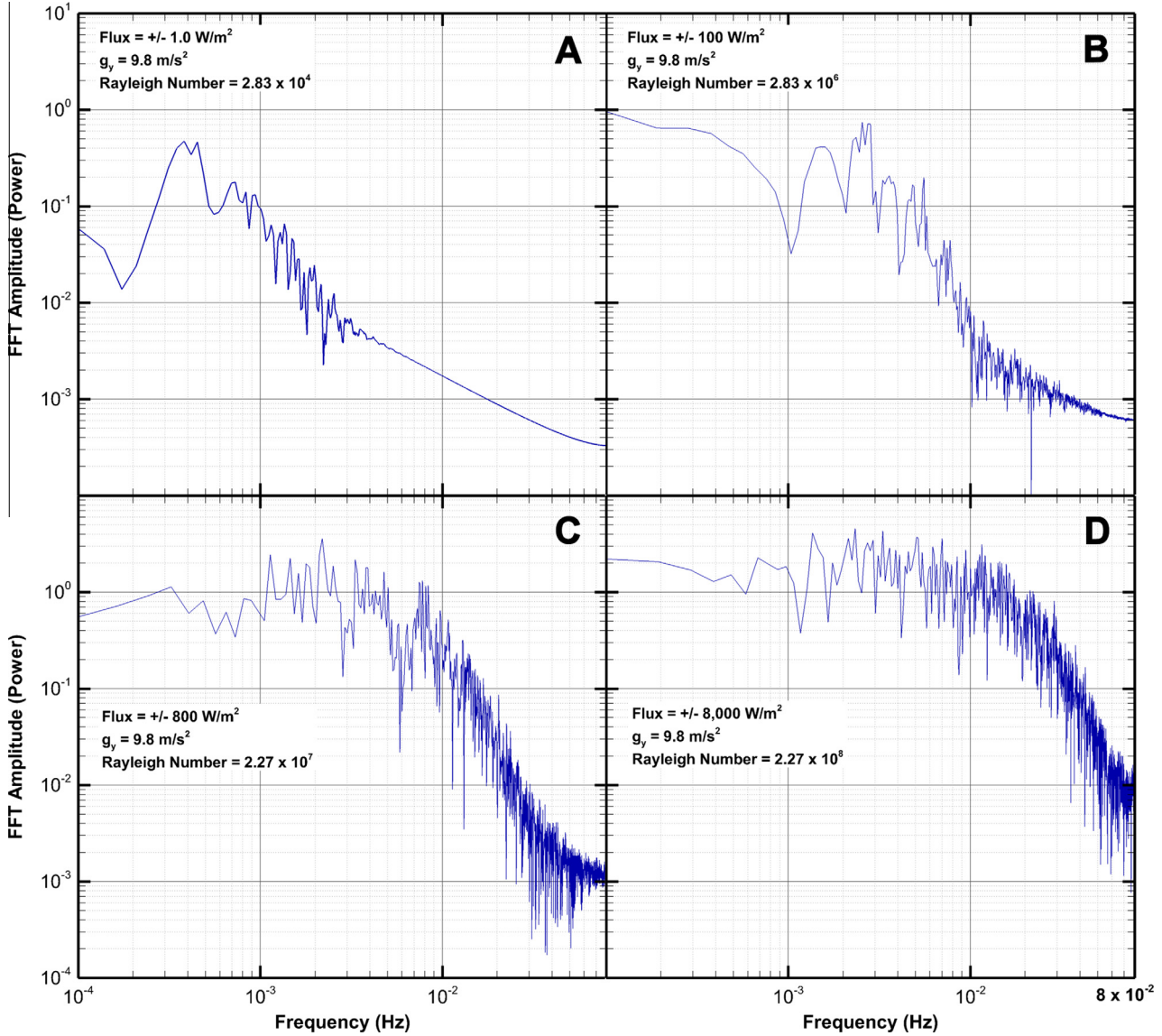


**Fig. 12.** A summary plot of the FFT power spectrum of the mass flow evolutions: (A) the stable oscillatory, decaying flow shown in Fig. 5; (B) the low forcing, weakly chaotic flow shown in Fig. 7; (C) the high forcing chaotic flow shown in Fig. 9; and (D) a high forcing chaotic flow regime at  $Ra = 2.27 \times 10^8$ .

The average time in which the thermosyphon resides in either the CW or CCW directions prior to experiencing a flow reversal has been measured from mass-flow time-series simulation data and is characterized in Fig. 14 on a log-log plot for both 2D and 3D geometries as a function of the Rayleigh number. In general, the residence time scales as  $Ra^{-0.41}$  as shown on the figure. For  $Ra < 5.67 \times 10^6$  the toroidal thermosyphon does not experience flow reversals and thus the residence time is not applicable. For  $Ra > 5.67 \times 10^6$ , the 2D thermosyphon is in a high-Rayleigh, aperiodic, stable flow regime and the only flow reversals observed are of the transient, start-up kind [25] and thus the 2D curve exhibits the sharp rise in residence time as shown in Fig. 14. It is worthy of note that, for increasing Rayleigh numbers, as the 2D thermosyphon enters the high Rayleigh, stable regime at  $Ra = 5.67 \times 10^6$ , the 3D toroidal thermosyphon enters the chaotic flow regime and the trend of residence time scaling as  $Ra^{-0.41}$  is maintained from 2D to 3D geometries. Furthermore, there is no high-Rayleigh, stable flow regime found for the 3D geometry as discussed in Section 4.2 above.

#### 4.4. Flow regime delineation

We end our discussion of results by delineating the various flow regimes according the forcing in the system as a function of the Rayleigh number. Fig. 15 shows a flow regime bifurcation diagram in the gravity vs. heat flux parametric space with lines of constant Rayleigh number superimposed. Note that the Rayleigh number scale is shown on the upper horizontal axis in Fig. 15 with curves of constant  $Ra$  emanating from said axis. Flow regimes have been characterized and delineated for all 2D and 3D cases discussed in this study.

From Fig. 15 it can be seen that, in general, the flow regime transitions in 3D reside at  $10\times$  the forcing of the 2D counterpart. For example, 2D stable convection begins at  $Ra \approx 5 \times 10^4$  whereas in 3D stable convection does not begin until  $Ra \approx 5 \times 10^5$ . Similarly, the onset of chaotic flow behavior in 2D occurs at  $Ra \approx 5 \times 10^5$  while chaotic flow in the toroidal geometry is suppressed to  $Ra \approx 5 \times 10^6$ . It is thus apparent that additional forcing is required in toroidal thermosyphons owing to the increased dissipation of additional

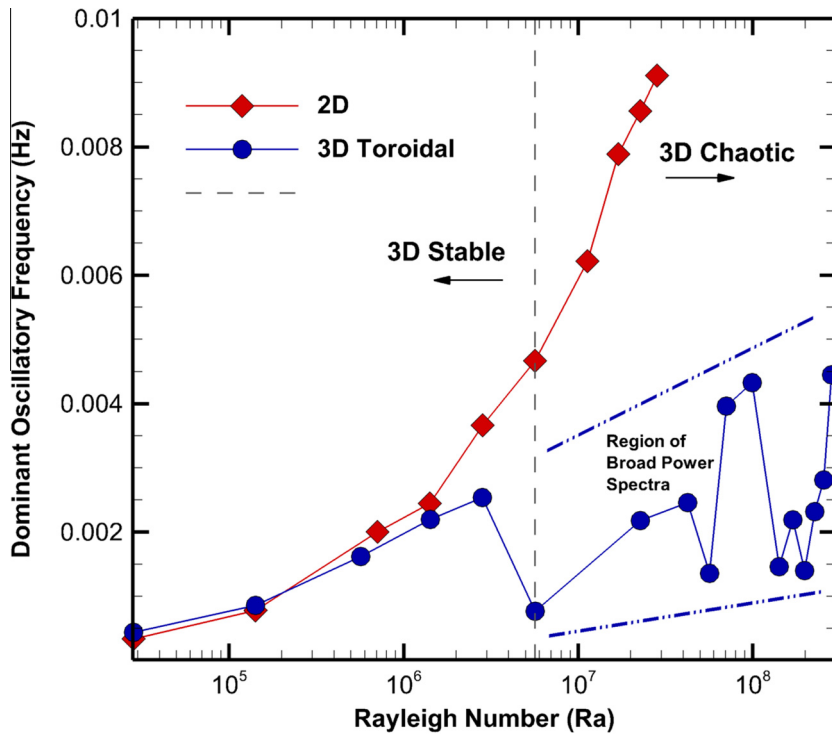


**Fig. 13.** A comparison of the dominant oscillatory frequency as a function of Rayleigh number for 2D and 3D toroidal thermosyphons. Note that 3D chaotic flows do not exhibit a well defined oscillatory frequency but rather a region of broad-band power spectra.

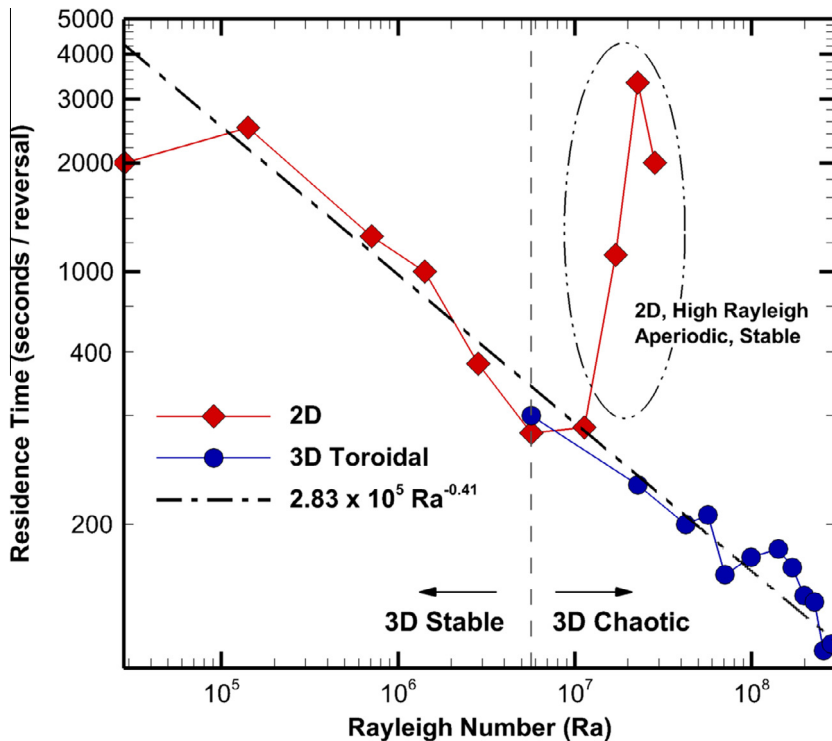


**Fig. 14.** A plot of the flow-direction residence-time as a function of the Rayleigh number. The spike in residence time for 2D cases corresponds to the high Rayleigh, stable flow regime not observed in 3D simulations. In general, the residence time scales as  $Ra^{-0.41}$  for both 2D and toroidal thermosyphons.

surface boundaries in fully 3D simulations. Furthermore, it is essential to note that while high-Rayleigh, aperiodic, stable convection is observed at  $Ra \approx 2 \times 10^7$  in 2D simulations, this regime is not found

in 3D toroidal simulations up through  $Ra = 2.83 \times 10^8$  and thus the factor of  $10\times$  does not appear to be valid for the return of high Rayleigh, stable convection for 3D geometries.

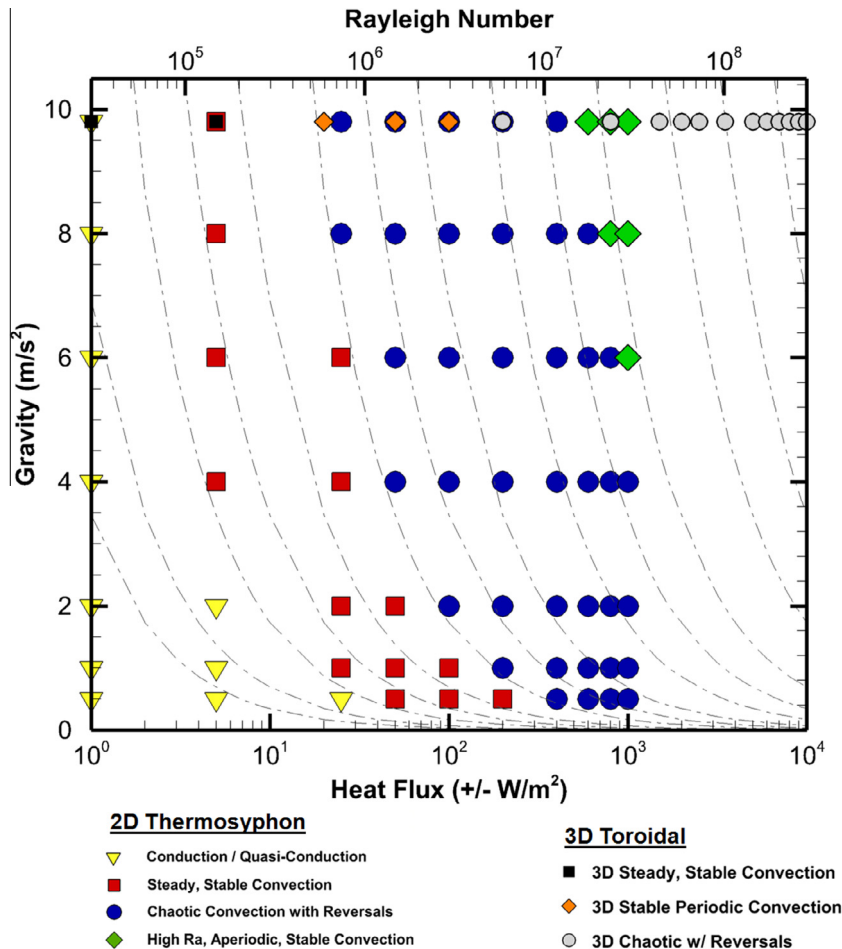


**Fig. 15.** A flow regime bifurcation diagram for both 2D and 3D thermosyphons as a function of Rayleigh number with gravity and heat flux as shown. Note that the high Rayleigh, aperiodic, stable convective regime is not found for 3D toroidal thermosyphons up to  $Ra \sim 10^8$ .

## 5. Conclusions

In this study, we have numerically modeled a 3D thermosyphon convection loop with toroidal geometry where an iso-heat flux boundary condition has been employed to provide buoyant forcing in a gravitational field. While prior 3D studies with an isothermal boundary condition did not demonstrate chaotic behavior nor flow reversals [23], here we find that the heat flux boundary condition did indeed produce an unstable, convective flow regime characterized by chaotic flow reversals. However, a stable, high-Rayleigh number convection regime was not observed with heat flux boundaries.

The dimensionless Rayleigh number has been shown to accurately capture the physics of the flow and fully characterize the observed behavior. Thermosyphon behavior has thus been characterized in terms the Rayleigh number according to the following: (1) the RMS wall temperature; (2) the temporal evolution and the RMS of the mass flow rate signal along with the associated attractor plots; (3) a frequency analysis including power spectrum, dominant frequency, and residence time; and (4) a flow regime bifurcation diagram. Computational results have also been compared to prior 2D thermosyphon data from the literature with iso-heat flux boundary conditions in order to provide insight to the reader.

When comparing 2D and 3D simulation results with heat flux boundaries, there are a few disparities that are worthy of note. First, all convective 2D simulations, including the stable, non-reversing flow regimes, exhibit one or more transient flow

reversals during establishment of the initial convective flow [25]; these transient reversals are not observed in any 3D toroidal simulations. Second, flow regime delineation in 3D generally occurs at a Rayleigh number that is  $10\times$  that of the comparable 2D simulation owing to the increased dissipation from additional solid boundaries in the confined 3D toroidal geometry. Finally, numerical results show that only three of the four distinct flow regimes exist in 3D toroidal thermosyphons, namely: (1) conduction, (2) damped, stable convection without flow reversals, and (3) Lorenz-like chaotic convection with flow reversals; there is no high-Rayleigh, stable convective regime observed in 3D systems for thermal forcing up to the limit where phase change begins ( $Ra \approx 2 \times 10^8$ ). In comparison, for 2D thermosyphon systems, the high Rayleigh, stable convective regime is observed at  $Ra > 2 \times 10^7$ .

Analysis of the mass-flow time-series data indicate that the RMS of the bulk mass circulation depends solely on the Rayleigh number as  $Ra^{0.41}$  and is consistent in both 2D and 3D systems. A comparison of the power spectra generated from the mass-flow time-series signal shows strong agreement of the dominant oscillatory frequency up to  $Ra \approx 3 \times 10^6$  at which point the trends diverge. For  $Ra > 3.0 \times 10^6$ , the 2D thermosyphon reveals a dominant oscillatory frequency that becomes more pronounced and increases with  $Ra$  while the toroidal thermosyphon exhibits broad-band power spectra. The residence time in a particular circulation direction for both 2D and 3D systems show excellent agreement with the general trend as  $1/Ra^{0.41}$ ; the notable exception is the 2D

thermosyphon diverging from this trend as it enters the high Rayleigh, aperiodic, stable convection regime that is not found in the toroidal geometry.

## Conflict of interest

None declared.

## Acknowledgment

This research was supported by a NASA EPSCoR Grant and NSF Grant #DMS-0940271 to CMD as a member of the Mathematics and Climate Research Network. It was also supported by the Vermont Advanced Computing Core and the Vermont Complex Systems Center.

## Appendix A. Supplementary data

Supplementary data associated with this article can be found, in the online version, at <http://dx.doi.org/10.1016/j.ijheatmasstransfer.2015.04.060>.

## References

- [1] C. Kent, *Condie Plate Tectonics and Crustal Evolution*, fourth ed., Butterworth-Heinemann Elsevier Science, 1997 (pp. 122–123).
- [2] John M. Wallace, David S. Gutzler, Teleconnections in the geopotential height field during the Northern Hemisphere winter monthly weather review, *Am. Meteorol. Soc.* 109 (4) (1981) 784812.
- [3] Walker S. Ashley, Thomas L. Mote, Mace L. Bentley, On the episodic nature of derecho-producing convective systems in the United States, *Int. J. Climatol.* vol. 25 (14) (2005).
- [4] Robert H. Johns, William D. Hirt, Derechos: widespread convectively induced windstorms, *Weather Forecasting* 2 (1987) 32–49.
- [5] Ron W. Przybylinski, The bow echo: observations, numerical simulations, and severe weather detection methods, *Weather Forecasting* 10 (June 1995) 203–218.
- [6] A. Mertol, R. Greif, A review of natural circulation loops, S. Kakac et al., (Ed.), *Handbook of Natural Convection: Fundamentals and Applications*, Hemisphere, Washington, D.C., 1985, pp. 1033–1071.
- [7] R. Greif, Natural circulation loops, *ASME J. Heat Transfer* 110 (1988) 1243–1258.
- [8] Y. Zvirin, A review of natural circulation loops in pressurized water reactors and other systems, *Nucl. Eng. Des.* 67 (1981) 203–225.
- [9] E.N. Lorenz, Deterministic nonperiodic flow, *J. Atmos. Sci.* 20 (1963).
- [10] K.D. Harris, E.-H. Ridouane, D.L. Hitt, C.M. Danforth, Predicting flow reversals in chaotic natural convection using data assimilation, *Tellus A* 64 (2012) 17598.
- [11] K.T. Yang, S. Kakac, Natural convection in enclosures, *Handbook of Single-Phase Heat Transfer*, Wiley, New York, 1987 (Chapter 13).
- [12] G.D. Raithby, K.G.T. Hollands, Natural convection, *Handbook of Heat Transfer*, third ed., McGraw-Hill, New York, 1998 (Chapter 4).
- [13] Y. Jaluria, Natural convection, *Heat Transfer Handbook*, Wiley, New York, 2003 (Chapter 7).
- [14] J.B. Keller, Periodic oscillations in a model of thermal convection, *J. Fluid Mech.* 26 (1966) 599–606.
- [15] P. Welander, On the oscillatory instability of a differentially heated fluid loop, *J. Fluid Mech.* 29 (1967).
- [16] M. Gorman, P.J. Widmann, K.A. Robins, Nonlinear dynamics of a convection loop: a quantitative comparison of experiment with theory, *Phys. D* 19 (1986) 255–267.
- [17] P.K. Vijayan, Experimental observations on the general trends of the steady state stability behavior of single-phase natural circulation loops, *Nucl. Eng. Des.* 215 (2002).
- [18] Y.Y. Jiang, M. Shoji, M. Naruse, Boundary condition effects on flow stability in a toroidal thermosyphon, *Int. J. Heat Fluid Flow* 23 (2002) 81–91.
- [19] Y.Y. Jiang, M. Shoji, Spatial and temporal stabilities of flow in a natural circulation loop: influences of thermal boundary condition, *ASME J. Heat Transfer* 125 (2003) 612–623.
- [20] G. Desrayaud, A. Fichera, M. Marcoux, Numerical investigation of natural convection in a 2D-annular closed-loop thermosyphon, *Int. J. Heat Fluid Flow* 27 (2006) 154–166.
- [21] H.F. Creveling, J.F. De Paz, J.Y. Baladi, R.J. Schoenhals, Stability characteristics of a single phase free convection loop, *J. Fluid Mech.* 67 (1975) 65–84.
- [22] E.H. Ridouane, C.M. Danforth, D.L. Hitt, A 2-D numerical study of chaotic flow in a natural convection loop, *Int. J. Heat Mass Transfer* 53 (2010) 76–84.
- [23] E.H. Ridouane, C.M. Danforth, D.L. Hitt, A numerical investigation of 3-D flow regimes in a toroidal natural convection loop, *Int. J. Heat Mass Transfer* 5 (2011) 5253–5261.
- [24] W.F. Louisos, D.L. Hitt, C.M. Danforth, Chaotic flow in a 2D natural convection loop with heat flux boundaries, *Proc. 43rd AIAA Thermophysics Conference*, New Orleans, Louisiana, June 25–28, 2012, Paper No. AIAA-2012-2752.
- [25] W.F. Louisos, D.L. Hitt, C.M. Danforth, Chaotic flow in a 2D natural convection loop with heat flux boundaries, *Int. J. Heat Mass Transfer* 61 (June 2013) 565–576.
- [26] FLUENT Manual, FLUENT Inc., 10 Cavendish Court, Centerra Resource Park, Lebanon, NH 03766, USA, 2006.
- [27] F.P. Incropera, D.P. Dewitt, *Fundamentals of Heat & Mass Transfer*, fourth ed., John Wiley & Sons, 1996.